Geochemistry Geophysics Geosystems G3

Published by AGU and the Geochemical Society

Article
Volume 13, Number 1
17 August 2012
Q08008, doi:10.1029/2012GC004157
ISSN: 1525-2027

Emplacement and dewatering of the world's largest exposed sand injectite complex

Timothy J. Sherry and Christie D. Rowe

Earth and Planetary Sciences, University of California, Santa Cruz, 1156 High Street, Santa Cruz, California 95064, USA

Now at Earth and Planetary Sciences, McGill University, 3450 University Street, Montreal, Quebec H3A 0E8, Canada (timothy.sherry@mail.mcgill.ca; christie.rowe@mcgill.ca)

James D. Kirkpatrick and Emily E. Brodsky

Earth and Planetary Sciences, University of California, Santa Cruz, 1156 High Street, Santa Cruz, California 95064, USA (jkirkpat@ucsc.edu; brodsky@es.ucsc.edu)

[1] Sandstone injectites form by up or down-section flow of a mobilized sand slurry through fractures in overlying rock. They act as reservoirs and high-permeability conduits through lower permeability rock in hydrocarbon systems. The Yellow Bank Creek Complex, Santa Cruz County, California is the largest known exposure of a sandstone injectite in the world. The complex contains granular textures that record processes of sand slurry flow, multiple pore fluids, and dewatering after emplacement. The injection was initially mobilized from a source containing both water and hydrocarbons. The water-sand slurry reached emplacement depth first, due to lower fluid viscosity. As the sand slurry emplaced, the transition from slurry flow to pore water percolation occurred. This transition resulted in preferred flow channels ~6 mm wide in which sand grains were weakly aligned (laminae). The hydrocarbon-sand slurry intruded the dewatering sands and locally deformed the laminae. Compaction of the injectite deposit and pore fluid escape caused spaced compaction bands and dewatering pipes which created convolutions of the laminae. The hydrocarbon-rich sand slurry is preserved today as dolomite-cemented sand with oil inclusions. The laminae in this injectite are easily detected due to preferential iron oxide-cementation of the well-aligned sand laminae, and lack of cement in the alternating laminae. Subtle textures like these may develop during sand flow and be present but difficult to detect in other settings. They may explain permeability anisotropy in other sand deposits.

Components: 3200 words, 8 figures.

Keywords: Peclet number; clastic injectite; granular flow; hydrocarbons; sand microstructure; soft sediment deformation.

Index Terms: 3022 Marine Geology and Geophysics: Marine sediments: processes and transport; 5104 Physical Properties of Rocks: Fracture and flow; 8169 Tectonophysics: Sedimentary basin processes.

Received 21 March 2012; **Revised** 13 June 2012; **Accepted** 17 June 2012; **Published** 17 August 2012.

Sherry, T. J., C. D. Rowe, J. D. Kirkpatrick, and E. E. Brodsky (2012), Emplacement and dewatering of the world's largest exposed sand injectite complex, *Geochem. Geophys. Geosyst.*, *13*, Q08008, doi:10.1029/2012GC004157.

1. Introduction

[2] Sand injectites form when a slurry of overpressured sand and fluid is mobilized and emplaced up or down-section through fractures in low permeability hostrock. Injectites provide high-permeability conduits between reservoirs separated by low-permeability caprock, and are of significant interest during oil and gas exploration and development, e.g., injectites seismically imaged in the North Sea oil fields [*Cartwright et al.*, 2007; *Hurst et al.*, 2003; *Hurst and Cartwright*, 2007; *Huuse et al.*, 2010; *Jonk et al.*, 2005]. Sand injectite complexes have been studied seismically [*Cartwright et al.*, 2008], by analog experiment [*Rodrigues et al.*, 2009; *Ross et al.*, 2011] and in outcrop exposures [*Hubbard et al.*, 2007; *Minisini and Schwartz*, 2006; *Schwartz et al.*, 2003; *Vigorito et al.*, 2008; *Vigorito and Hurst*, 2010]. These studies document the geometry of injectites and often interpret constraints on pressure and depth, and long-term permeability effects. However, few studies have directly investigated the dynamics of sand slurry flow and emplacement, as these processes are generally not thought to be preserved in the depositional record. Contributions have been made from studies of flow textures in injected sands, and scour features on the conduit walls [e.g., *Kane*, 2010] and mineral sorting and AMS fabrics developed by velocity gradients during injection [e.g., *Levi et al.*, 2006; *Kazerouni et al.*, 2011]. Mechanisms for triggering sand injections have also been studied, ranging from seismic waves [*Levi et al.*, 2008, 2011], to diagenetic changes in pore pressure [*Davies et al.*, 2006]. However, much remains to be learned about the dynamics of sand slurry flow and emplacement, as well as the dewatering processes which begin as the sand stops moving.

[3] The Yellow Bank Creek Complex, Santa Cruz County, California is the world's largest documented outcrop exposure by volume [*Thompson et al.*, 2007]. The largest of the sand injectites forms a thick sill exposed in ≥10 m high beach cliffs. This affords a unique opportunity to study the emplacement process of sand injectites, and to assess how the details of granular flow dynamics may be preserved in the rock record.

[4] A complex assemblage of textures are observed in the Yellow Bank Creek Complex, which have been the focus of two previous studies [*Scott et al.*, 2009; *Thompson et al.*, 2007]. These previous works promote conflicting hypotheses as to the origins of the sand textures, and their implications. We employed field and microstructural studies to quantitatively describe the exposure- and grain-scale fabrics of the Yellow Bank Creek Complex, interpret the sequence of events accompanying sand injection and emplacement, and resolve the remaining questions about the preserved textures. We relate these textures to the processes of sand flow, emplacement, jamming and dewatering. We then explore the implications of our results for the permeability structure of injected sands revealed in the laminae of the Yellow Bank Creek Complex.

2. Geologic Setting

[5] The Monterey Formation was deposited on the California coast in a northward-migrating transtensional basin along the San Andreas Fault system during the late Miocene [*Graham and Williams*, 1985] (Figure 1a). The formation is regionally important as the reservoir and source rock for the Monterey Formation oils [*Graham and Williams*, 1985]. The upper part of the formation is predominantly thin bedded diatomaceous mudstone [*Bramlette*, 1946]. However, in Monterey and Santa Cruz Counties, discontinuous well-sorted Santa Margarita Formation sands are interfingered in lenses near the top of the Monterey Formation [*Bramlette*, 1946]. Above the Santa Margarita Formation, the Monterey Formation is locally known as the Santa Cruz mudstone [*Boehm and Moore*, 2002] (Figure 1b).

[6] Sandstone injectites, sourced from the Santa Margarita sands, occur in the upper Monterey Formation, having injected upsection [*Stanley*, 1990; *Bramlette*, 1946]. The injectites form dikes, sills, and large amorphous bodies and, locally, appear to have been shallowly emplaced. Some of the injectites may have reached the paleo-seafloor as extrudites [*Boehm and Moore*, 2002]. Some of the sandstone injectites are tar-saturated, or cemented with dolomite containing bitumen [*Stanley and Lillis*, 2000]. Injectite ages may be constrained as the Santa Margarita Formation sands were deposited in the upper Miocene based on the ages of invertebrate fossils [*Addicott*, 1972] and vertebrate fossils [*Phillips*, 1981], and the unconformity separating the Santa Cruz Mudstone from the overlying Purisima Formation of late Miocene to late Pliocene based on fossil ages [*Clark*, 1981].

[7] Abundant evidence for fluid migration within the Monterey Formation and Santa Margarita sands has led to several theories for the driving forces causing the injectites. *Boehm and Moore* [2002]

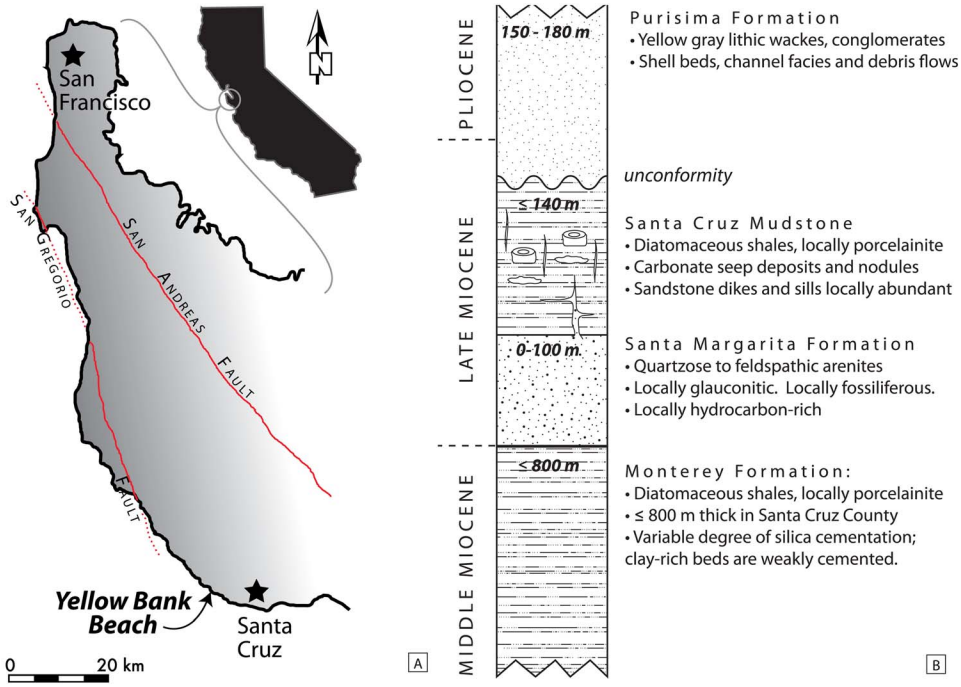

Figure 1. (a) Regional map showing location of Yellow Bank Beach relative to San Andreas and San Gregorio fault systems. (b) Regional stratigraphy modified from *Clark* [1981], *Scott et al.* [2009], *Stanley and Lillis* [2000], and *Thompson et al.* [2007].

argued that the position of the injectite complex toward the thin edge of a westward-deepening basin would have generated artesianal fluid overpressures as pore waters escaped updip from the more deeply buried strata to the west. Silica diagenesis in the diatomaceous Monterey Formation may have caused injectite formation by facilitating the reduction of porosity, increasing pore fluid pressure during opal de-watering [*Davies et al.*, 2008], and embrittlement of the mudstones [*Gross*, 1995]. Numerous authors have suggested seismic shaking may be a proximal trigger of the fluidization and injection of sand, especially given the basin's close proximity to both the San Andreas and San Gregorio fault systems, which were active in this area during the late Miocene when these formations were deposited [*Stanley and Lillis*, 2000; *Boehm and Moore*, 2002; *Thompson et al.*, 2007].

[8] The majority of the sand injectites in the area can be classified as single and cluster dikes, or sills, a few centimeters wide and several meters long. Injectite orientations suggest that the tectonic stresses affecting the region in the late Miocene were similar to today [*Boehm and Moore*, 2002].

[9] At Yellow Bank Beach, locally known as Panther Beach (located in Coast Dairies State Park, 10 km north of the Santa Cruz city limits), a unique, large-scale injection is exposed. The injection has a sill-like, tabular shape, and *Thompson et al.* [2007] estimated its total volume at 8.4×10^6 m^3. The complex contains both hydrocarbon-saturated and hydrocarbon-poor injectites [*Boehm and Moore*, 2002]. The Yellow Bank Creek Complex has attracted broad interest due to its size and the complexity of its internal fabrics [*Aiello*, 2005; *Scott et al.*, 2009; *Thompson et al.*, 2007]. The maximum burial depth of the Santa Cruz mudstone host rock to the injectite is well constrained. Apatite fission track studies by *Thompson et al.* [2007] and estimates of burial temperature from silica diagenesis by *El-Sabbagh and Garrison* [1990] suggest the formation reached depths and temperatures of 1.3–1.6 km and 45–50°C. Observations of this and other nearby sand injectites suggest that the long outcrop length in horizontal beach exposure is due to the intrusion of a sill, subparallel to the paleoseafloor, sourced from a wide dike of sand that migrated vertically up-section [*Phillips*, 1990].

3. Previous Work

[10] Previous studies of the Yellow Bank Creek Complex described the complex fabrics that characterize this outcrop. These fabrics are described in detail in following sections. Sand cemented with

dark gray, hydrocarbon-rich dolomite forms rounded and columnar bodies with sharp boundaries within the injectite. The sand around these dolomite-cemented areas is weakly cemented. Iron oxide cement stains alternating laminae (~5–10 mm thick), which are locally organized into zones 10–20 cm thick called layers by *Thompson et al.* [2007] and bands by *Scott et al.* [2009]. The thin laminae are ubiquitous and usually sub-horizontal, while the coarser bands vary in orientation, cut margins between laminated and dolomite sands, and are well developed only near the edges and base of the injectite [*Thompson et al.*, 2007]. Clasts of the mudstone host rock are included in the injectite, and are particularly abundant near the edges.

[11] The origins of the fabrics and different cements in the Yellow Bank Creek Complex are ambiguous. Previous authors have presented two different interpretations. Based on outcrop observations, *Thompson et al.* [2007] argued that the 10-cm bands were flow bands formed during sand injection, and the rhythmic iron oxide cementation was Liesegang banding formed during groundwater flow through the injectite long after emplacement. However, they also noted that the relative chronology of the two fabrics is sometimes unclear. Dolomite cement is interpreted to have formed by bacterial action when either oil displaced pore water in the sands, without disrupting the surrounding granular structure, or during the intrusion of an oil supported slurry into previously emplaced water-saturated sands [*Thompson et al.*, 2007]. *Scott et al.* [2009] described the same fabrics, but used qualitative microstructural observations to develop a different interpretation of their origins. Based on the evidence for corrosion of the mudstone host rock, *Scott et al.* [2009] argue convincingly that the sand was injected as a high velocity turbulent flow, and the preserved laminae and layering record late-emplacement processes. They report that the mm-scale laminae are defined by a difference in grain packing (porosity), and therefore argue that the iron oxide cement overprints on a primary grain fabric formed during injection of the sand, not by Liesegang instabilities as suggested by *Thompson et al.* [2007]. *Scott et al.* [2009] suggest that the 10–20 cm banding was formed by shearing within the sand body while in a semi-consolidated state.

4. Field Observations

[12] The striking outcrop appearance of the Yellow Bank Creek Complex is due to the juxtaposition of different granular fabrics and two types of boldly colored mineral cements (Figure 2a). We give morphological descriptions of these features to establish terminology, document the crosscutting relationships between various features, and present quantitative observations of fabrics on outcrop to thin-section scale. The injectite outcrops along ~170 m of beach cliffs that are ~10 m high.

4.1. Laminae

[13] The most ubiquitous fabric of the injectite is the ~6 mm thick laminae (Figures 2, 3, and 5) (previously described by *Scott et al.* [2009] and *Thompson et al.* [2007]). This fabric is defined by thin, alternating laminae of iron oxide-cemented and uncemented sand. The laminae are always locally parallel and consistent in thickness. Iron oxide-cemented laminae are typically slightly thinner than the uncemented laminae in between. The laminae are wavy and undulating on wavelengths of a few centimeters to 10 s meters (Figure 2). They are pervasive throughout the outcrop of the large sand injectite, but are absent from the thinner (≤1 m) sand dikes in the area, which are massive or show wall-parallel grain size gradients [*Thompson et al.*, 2007]. The laminae thickness across the entire outcrop is $\sim 5.7 \pm 1$ mm (1σ); $N = 697$. Iron oxide-cemented laminae are more resistant than uncemented laminae and subtly stand out as positive erosional features.

[14] The dolomite-cemented sand does not contain the iron oxide cements which elsewhere define and emphasize the laminae. In some areas, the dolomite-cemented columns sharply cut across laminae (Figure 3), while in others, the laminae are curved toward small dolomite cemented bodies (Figure 2b). In either case, the laminae appear to be deformed by the dolomite-cemented sand bodies.

4.2. Mudstone Clasts

[15] Clasts of Santa Cruz Mudstone are observed within the both dolomite-cemented and laminated sands (Figures 2c and 2d). These were described by *Scott et al.* [2009] and by *Thompson et al.* [2007] as sedimentary xenoliths. The mudstone host rock is strongly bedded, contributing to an abundance of elongated clast shapes (Figure 2c) with some larger clasts containing intact bedding planes. We measured clast long and short axes on the outcrop surface (Figure 4). The clasts range in size from sand-sized grains to ~70 cm, but most of the observed clasts are a few centimeters. As reported by *Scott et al.* [2009], the clasts are more abundant close to the injectite margins. The observation that many

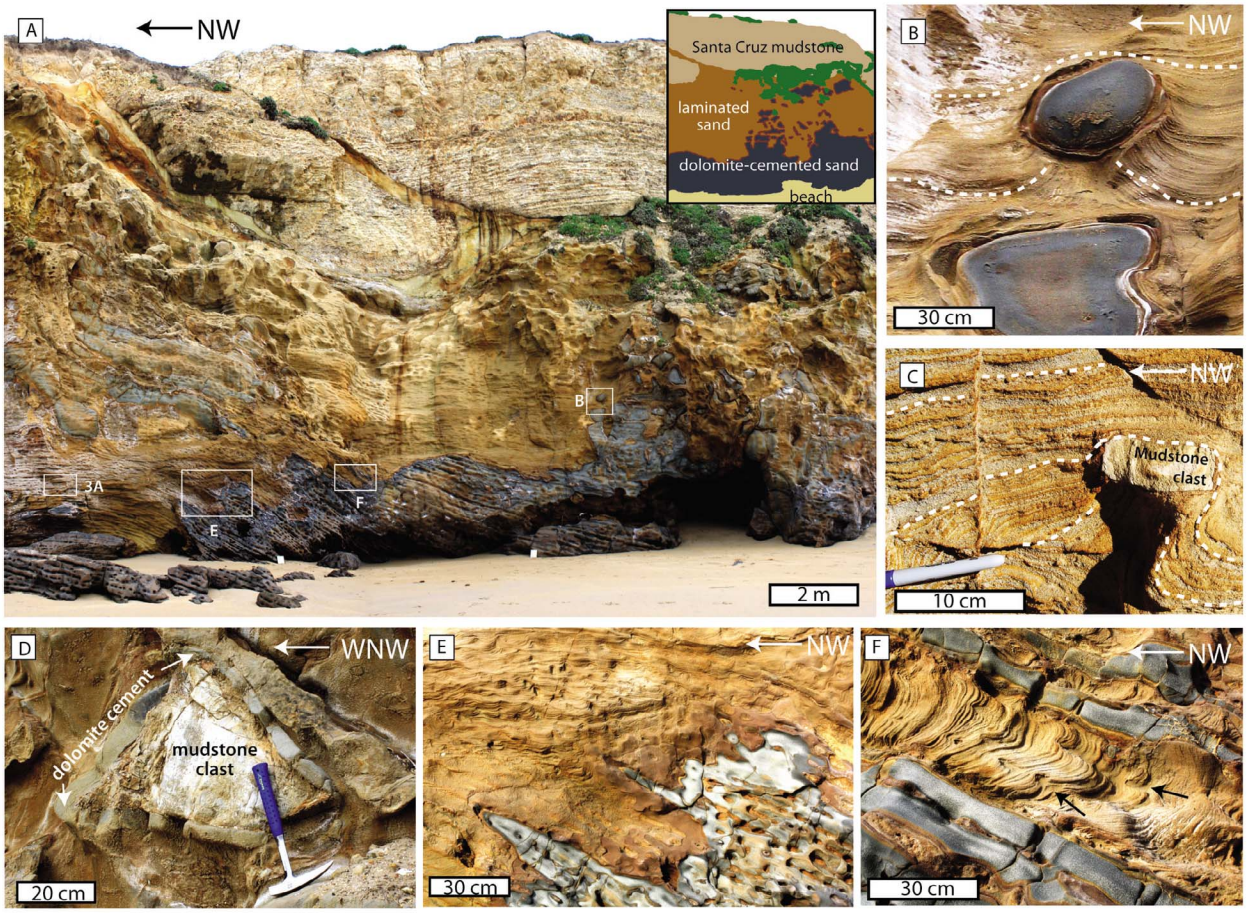

Figure 2. (a) Overview of the Yellow Bank Creek Complex outcrop. Undulating roof of injectite is exposed (ceiling is host rock Santa Cruz Mudstone). Small sand dyke injects from top of injectite at center toward upper left of photo. Majority of exposed sand injectite is laminated with iron oxide cement (appears yellow in photo). Dolomite-cemented, bitumen-rich sandstone is exposed at beach level and forms rounded columns and bubble shapes leading to "lava lamp"-like appearance. White patches on lower part of outcrop are salt from wind-blown sea spray. Locations of Figures 2b, 2e, 2f, and 3a are indicated. (b) Relationship between dolomite-cemented and laminated sandstone. Rounded body of dolomite-cemented sandstone distorts laminae in laminated sand (dashed white lines trace deformed laminae). (c) Iron oxide-cemented laminae distorted around a mudstone clast within sand injectite. Dashed white lines trace laminae. At center left, a vertical deformation band in the sandstone offsets the laminae and is preferentially iron oxide cemented, establishing relative chronology. Mudstone clast is at a low angle to laminae to the left. (d) Largest exposed mudstone clast in the injectite. Clast has rim of dolomite-cemented sandstone which is surrounded by iron oxide-cemented laminated sand. (e) Banding cutting across contacts between dolomite-cemented and laminated sand. (f) Steeply dipping laminae between bands of dolomite-cemented sand. Convolute structures (black arrows) deform laminae with antiforms pointing laterally toward upper left of photo.

clasts are rounded, saturated with hydrocarbons, and have dolomite sand rims (e.g., Figure 2d) supports the hypothesis that the mudstone clasts were not all locally derived, as the exposed wall rock to the injection is relatively hydrocarbon-poor. This is consistent with *Scott et al.*'s [2009] interpretation of significant vertical transport of the clasts during rapid upward injection of the sand slurry.

[16] We compared the clast size and orientation of the long axis of the elongate mudstone clasts to the orientation of the laminae around each clast to determine whether the clasts and the laminae were locally parallel (Figure 4). Of the 27 elongate clasts, 50% have their long axis aligned within 10° to the local laminae. The other 50% have long axis at an angle of 10–50° to the laminae. The rakes of mudstone clast long axes measured in the outcrop surface have a wide distribution of angles for any given location along the exposure. Mudstone clasts are sub-horizontal (mean apparent plunge of long axis = 17° ± 17°, N = 82). There is no apparent

Figure 3. Dolomite-cemented sandstone columns crosscutting laminae. Hammer for scale.

relationship between clast size, aspect ratio, and orientation relative to local laminae. The laminae wrap around the mudstone clasts, never terminating against them.

4.3. Dolomite Cemented Sand

[17] The most noticeable feature of the injectite in outcrop is the contrast between the laminated orange-yellow sand and the lava lamp-like, circular, elongate blue-gray blobs and columns of hydrocarbon-rich dolomite cement (Figures 2 and 3). The contacts between regions of different cement are smoothly curved and sharp. Dolomite cemented bodies strongly resemble bubbles in shape, have consistent sense and radius of curvature, and are aligned in vertical columns or trains (Figures 2a, 2b, and 3). There is a rim of maroon-colored hematite cement ~2 cm thick forming a cortex around the margins of dolomite-cemented regions (Figure 2b). The laminae are crosscut by or deformed by contacts between laminated and dolomite-cemented sand (Figures 2b and 3).

4.4. Banding

[18] Six to thirteen cm-spaced *bands* deform both laminated and dolomite cemented sand across the outcrop. The bands are most strongly expressed in laminated sand as ~1–2 cm wide layers where the laminae are more closely spaced (Figure 5a). These bands are more erosion-resistant due to a concentration of iron oxide cement and stand out from the outcrop surface. The laminae locally deflect to become more parallel and planar in the bands, relative to the general wavy style (Figure 5a). This foliation was called "layers" by *Thompson et al.* [2007] and "bands" by *Scott et al.* [2009]. The banding also occurs in the dolomite-cemented sandstone, where bands preferentially weather back creating aligned indentations in the outcrop surface (Figure 2e). In some areas, bands cut across the boundaries between laminated sand and dolomite-cemented sand (Figures 2a and 2e).

[19] The bands are locally planar, but undulate on wavelengths of several meters. They are strongly developed in some parts of the injectite (Figure 5a),

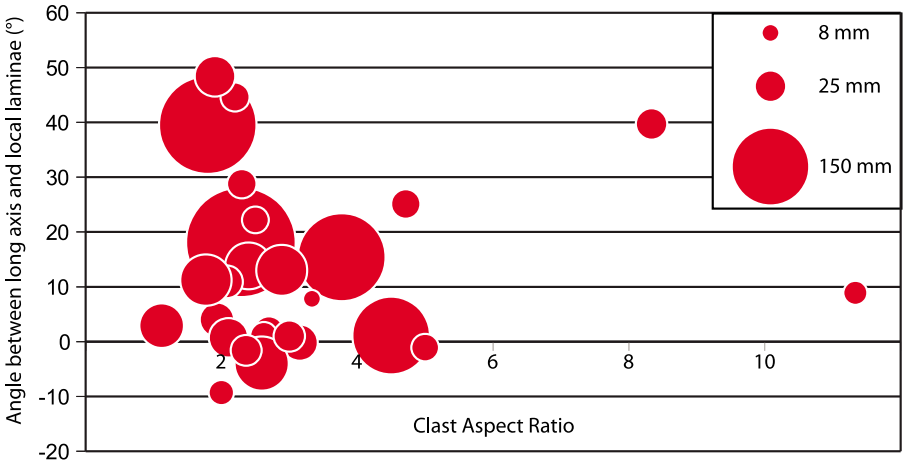

Figure 4. Geometry of the mudstone clasts. Horizontal axis: Aspect ratio of mudstone clast. Vertical axis: local angle between the long axis of the mudstone clast and the laminae in the surrounding sand. Symbol size scaled by equivalent diameter. None of these three measurements co-vary. N = 27.

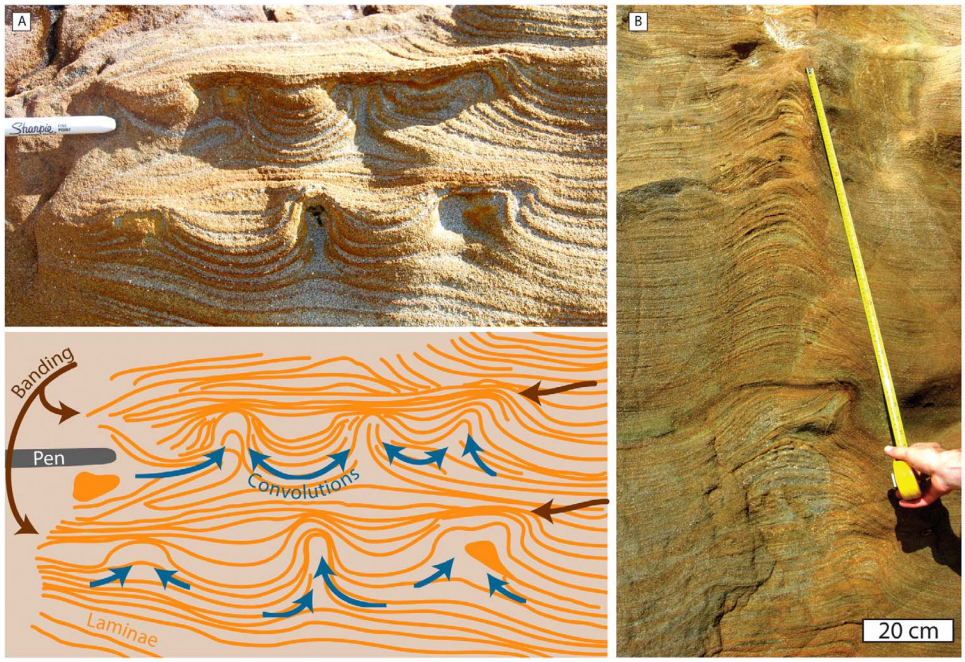

Figure 5. (a) Outcrop photo showing relationship between laminae, bands and convolutions. Sub-horizontal, ≈6 mm *laminae* (orange lines in cartoon) are differentially iron oxide-cemented. Closer spacing of iron oxide-cemented laminae in spaced surfaces create ≈10 cm *banding* (brown arrows). Antiformal undulations of the laminae create *convolutions* (blue arrows) which are confined between bands. (b) In other areas along outcrop where banding is not present laminae are deformed as convolution structures where axial reach is not limited into banding. We interpret these relationships to show that laminae predate both banding and convolutions.

and weak or absent in other parts (Figure 5b). They are generally subhorizontal or gently dipping but steepen dramatically at the northern end of the outcrop in the proximity of a fault. *Thompson et al.* [2007] proposed that bands generally follow the roughness of the floor of the injectite, but we could not confirm this as the floor is not locally exposed.

4.5. Convolutions

[20] The laminae locally show regularly spaced upward undulations creating antiformal deflections (Figures 2f and 5). These were described as "convolute lamination" by *Thompson et al.* [2007] and as "pipes" by *Scott et al.* [2009]. The lower edge of each feature is emergent and the amplitude of deflection increases upward (Figure 5b). As noted by *Scott et al.* [2009], the center of each feature is massive (i.e. the laminae are "washed-out" in the middle, Figure 5a). The upper terminations of the features are sharp, with a sudden transition from a strongly deflected lamination to smooth, parallel laminae. The tops are either concentric (i.e. center of Figure 5a) or flattened to a rectangular shape against the overlying band (i.e. right side of center band, Figure 5a). These shapes are accommodated by changes in the spacing and size of the laminae, similar to the bands described above. Each individual lamination is continuous across the convolution feature (i.e. the number of laminae on each side of the center "washout" is typically the same).

[21] Where the banding is strongly developed, the antiformal convolutions are limited in axial trace length (or vertical "reach") to the distance between two adjacent bands (Figure 5a). In this case, the convolutions are closely and regularly spaced, similar in amplitude, and recur within each space between bands. The axial planes are not always normal to the bands, as in Figure 2f, where axial trace is near parallel (upper left to lower right in photo) to banding. Convolutions are sometimes cut or confined by dolomite cemented sandstone bodies (Figure 2f). Where banding is absent, the vertical reach of the convolutions is not limited and has a vertical extent of ~0.5–1.5 m or greater (Figure 5b). Upward deflections of laminae were observed below mudstone clasts (Figure 2c).

4.6. Summary of Crosscutting Relations

[22] Below we review the individual features of the Yellow Bank Creek Complex, highlighting crosscutting relationships.

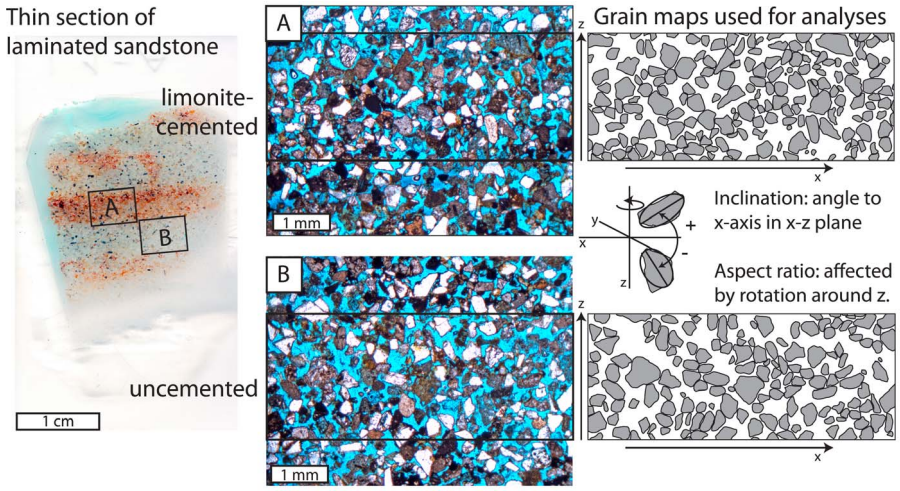

Figure 6. From photomicrographs of (a) iron oxide-cemented and (b) uncemented laminae, subareas were defined which lie completely within a single lamination. Grains in the subareas were outlined in Adobe Illustrator to facilitate analysis. Using the method of *Bjørk et al.* [2009], best fit ellipses were applied to grains and the inclination angle between long axis and horizontal was measured (sign conventions are shown). Angles were measured from top edge of the subset area, parallel to laminae.

[23] 1. Mudstone clasts are included within both laminated and dolomite-cemented sandstones. Laminae (~6 mm thick sub-horizontal alternating layers of iron oxide cemented and uncemented sand) are pervasive throughout the injectite except in dolomite-cemented areas. Laminae wrap concentrically around mudstone clasts.

[24] 2. Column or bubble-shaped dolomite-cemented sandstone bodies cut and deform laminae.

[25] 3. Banding (spaced compaction bands expressed by decreasing spacing of the laminae) and convolutions (antiformal undulations of laminae) are both defined by changes to the laminae geometry. They formed roughly simultaneously, perhaps with banding initiating prior to convolutions. Convolutions terminate against banding where both features are present. Isolated convolutions occur where banding is not expressed. Convolutions are sometimes confined between two dolomite-cemented sandstone bodies.

5. Microstructural Observations

[26] Laminae were described by *Thompson et al.* [2007] and interpreted as Liesegang banding, or concentric oscillations in cementation within homogeneous rock. *Scott et al.* [2009] argued that fluctuations in packing density of the sand grains are responsible for the laminae, and the iron-oxides preferentially precipitated in the lower-porosity bands. To test these hypotheses, we have used image analysis of photomicrographs to quantify the grain size distribution, packing density, and grain inclination patterns, for comparison between the two laminae types: uncemented versus iron oxide cemented.

[27] Thin sections were prepared from oriented samples in which the two laminae could be easily distinguished. Photomicrographs at 1.6× magnification were taken of representative areas of the samples in both plane-polarized and cross-polarized light with the edge of the photomicrographs parallel to the laminae in the section. From these photomicrographs, iron oxide cemented and uncemented sub-areas were selected from within the laminae for image analysis (Figure 6). Grains and impressions in the epoxy showing where grains were plucked during polishing were selected manually from each sub-area. The resulting grain maps were analyzed following the method of *Bjørk et al.* [2009]. Grains were automatically detected in the image by specifying the gray scale value used to construct the grain maps. Each grain was assigned a unique identity and the area was calculated from the number of pixels comprising each grain. Two-dimensional porosity (apparent porosity) was calculated by subtracting the sum of pixels within detected grains from the total pixels in the image. Pore space and mineral cements (dolomite or iron oxide) were therefore combined to represent primary porosity. An ellipse of equal area to each grain and with the long axis orientation specified by the second

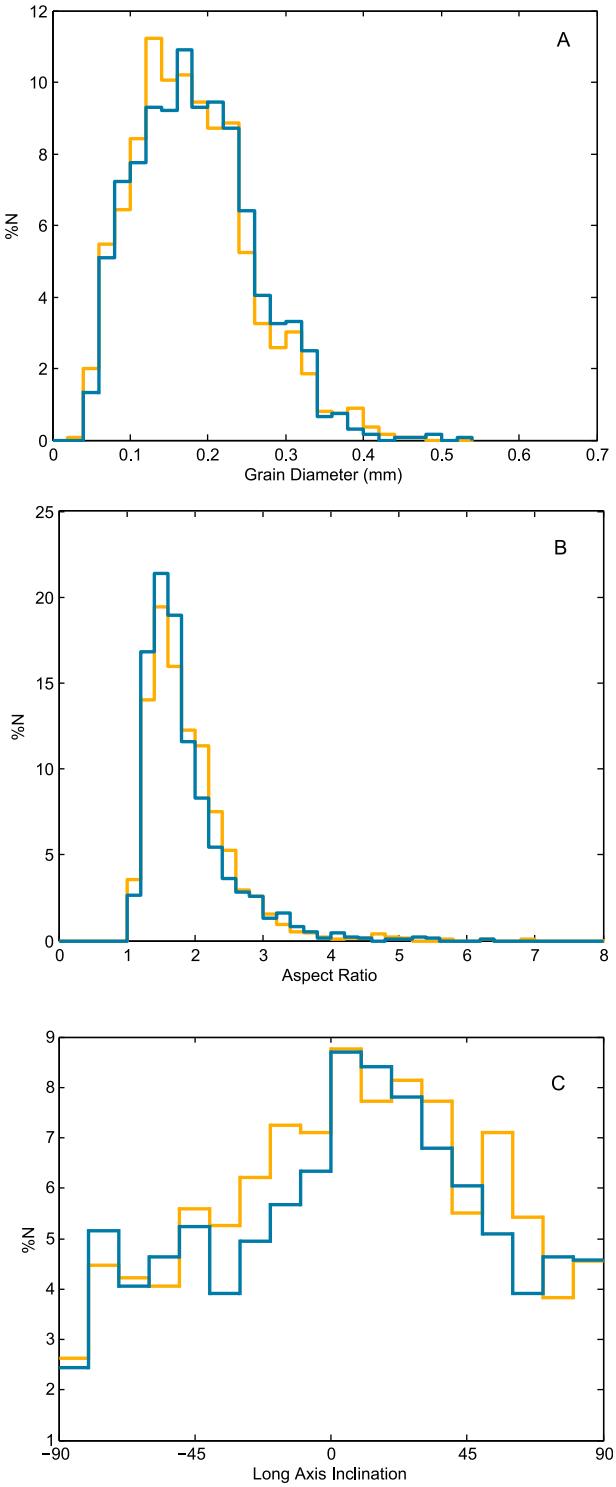

Figure 7. Histograms showing apparent grain diameter, grain aspect ratios, and grain inclination for iron oxide-cemented and uncemented laminae. All data are normalized to the total number of grains counted in each type of laminae.

moment of the grain pixel distribution was assigned to each grain (Figure 6). The angle between the long axis of each grain and the local surface of the iron oxide-cemented laminae was measured (orientation in x-z plane, Figure 6). Inclinations counter-clockwise from horizontal are positive, and clockwise from horizontal are negative. The aspect ratio of grains was calculated from the long and short axes of the best fit ellipses. The aspect ratio seen in the 2D section is a function of the true aspect ratio of the grain, as well as the orientation of the grain within the plane of the laminae (x-y plane, Figure 6).

[28] Analysis of eight sub-areas from within the iron oxide-stained laminae yields a mean apparent porosity of 51.3 $\pm$ 2.8% (1σ) with porosity values ranging from 57% to 48%. Eight sub-areas from within uncemented laminae define a mean apparent porosity of 47.8 $\pm$ 3.0% (1σ) with porosity values ranging from 51% to 43%. Kolmogrov-Smirnov tests with a 5% (p-value = 0.05) significance threshold were performed to compare distributions between laminae types. The Kolmogorov-Smirnov test showed the porosities of the iron oxide-cemented and uncemented laminae are indistinguishable (p-value = 0.18). The sand is composed of quartz, lithics, plagioclase feldspar, glauconite, carbonate fragments, and mud pelloids. We detected no grain compositional difference between iron oxide-cemented and non-cemented layers. The apparent porosity values are derived from 2D section through the sandstone. The high apparent porosity values are reasonable as 3D porosity is on the same order of magnitude but slightly lower than apparent 2D porosity in typical sands [*Long et al.*, 2009; *Keehm et al.*, 2004].

[29] A total of 1354 grains were counted in the selected regions within the iron oxide laminae and 1356 grains in the non-cemented laminae. The minimum apparent 2D grain diameter detected by our method is 2.6 $\times$ 10^{-2} mm and the maximum is 0.54 mm. Apparent grain diameter is a proxy for grain size (Figure 7a).

[30] Mean uncemented and iron oxide-cemented apparent grain diameter are 0.17 mm $\pm$ 0.07 (1σ) and 0.17 mm $\pm$ 0.08 (1σ), respectively. The two sets of grain size measurements have similar distributions (p-value = 0.87). Therefore, we observe no differentiation in grain size between uncemented and iron oxide-cemented laminae.

[31] Apparent grain aspect ratios, defined by the ratio of the major and minor axes of the equivalent

area ellipse, were analyzed (Figure 7b). Apparent aspect ratios in both iron oxide-cemented and non-cemented laminae fall mostly between one and two. Mean aspect ratios for non-cemented and iron oxide-cemented grains are 1.77 ± 0.6 (1σ) and 1.81 ± 0.70 (1σ). The Kolmogorov-Smirnov test confirmed a small, but significant difference between the aspect ratios of sand grains in uncemented laminae and sand grains in the iron oxide-cemented laminae (p-value = 0.0014).

[32] The inclination of grains to the lamination was compared between the two populations (Figure 7c). Mean inclination angles for iron oxide-cemented and uncemented populations are 1.85 ± 46.7° (1σ) and 0.7 ± 47.6° (1σ). There is no difference in the populations (p-value = 0.63).

[33] The analysis of the microstructure of the sand demonstrates that subtle differences exist between the layers at the grain scale. They are indistinguishable when compared in terms of apparent porosity, grain size, and inclination of sand grains to the laminae. The only subtle but significant difference is found in the apparent aspect ratio.

6. Discussion

[34] A sand injectite such as the Yellow Bank Creek Complex, which is mobilized as a slurry, may go through two transitions in flow regime during emplacement. First, the velocity will decrease as it rises through cracks and relieves the driving pressure. If the slurry is initially turbulent as argued by *Scott et al.* [2009], the Reynolds number will consequently drop and the flow will transition from turbulent to laminar flow. Second, at the time of emplacement, the flow will transition from a "single-phase" fluid where sand and pore fluid are moving at approximately the same velocity, to a "jammed" state, in which the pore fluid velocity has dropped sufficiently that grains are no longer suspended, the number of contacts between grains increases exponentially, and the grains geometrically lock (Figure 8) [*Majmudar et al.*, 2007]. At this point, the *jamming transition*, the sand grains will stop moving and the pore fluid will flow

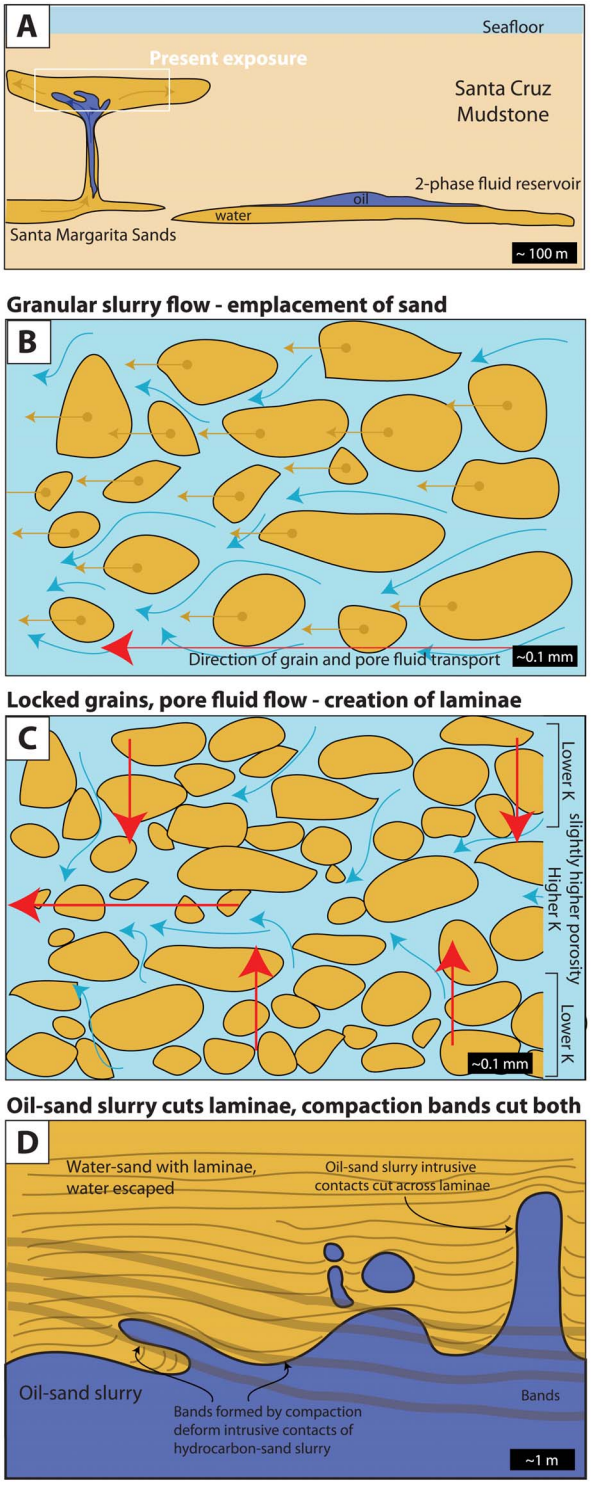

Figure 8. (a) Cartoon illustrating geometry of sand slurry injection from two-phase fluid reservoir. Cartoons illustrating transition from (b) granular flow to (c) pore-fluid flow at threshold velocity. Blue arrows show pore fluid flow paths, yellow arrows show granular transport path. Red arrows show general transport direction in Figure 8b and pore fluid escape direction in Figure 8c. (d) After the laminae formed, the slower oil-sand slurry intruded, deforming and crosscutting the laminae. The whole injectite body, fully emplaced, began to compact, forming bands and convolutions (Figure 8d). Compare to Figure 2.

through pore spaces, exerting a slight flow pressure on the grains.

[35] Below, we review the relative timing of development of each of the textural features described in the previous sections and then discuss the mechanisms by which they formed. We incorporate our new data, expanding upon the previous generalized emplacement interpretations to establish the emplacement history and relate the textural features to flow dynamics.

6.1. Injection Initiation

[36] Prior to injection, Santa Cruz mudstone overlay the Santa Margarita Formation whose pore fluids consisted of both aqueous and hydrocarbon phases. These were likely spatially separated, creating a two phase reservoir containing a region of water saturated sand and a region of oil sand (local outcrop examples of fluid phase boundaries were described by *Phillips* [1990]) (right side Figure 8a). Injection initiation may be caused by overpressure when the pore fluid pressure exceeded the hydrostatic pressure [*Jolly and Lonergan*, 2002] or when a triggering event occurred (e.g., seismic shaking or a change in lithostatic load caused by submarine slides [*Cartwright et al.*, 2008; *Cartwright*, 2010; *James et al.*, 2003; *Levi et al.*, 2006]).

[37] The emplacement depth of the Yellow Bank Creek Complex is unknown, but some observations and theory provide general constraints. *Thompson et al.* [1999] defined maximum burial depth from vitrinite reflectance data of Santa Cruz Mudstone near the complex and apatite fission track analyses of injectite sandstone (1.3–1.6 km assuming a geothermal gradient of ~30°C/km). Sand injectites are abundant in the area, mostly as small (10s cm) dikes with subsidiary sills [*Boehm and Moore*, 2002; *Jolly and Lonergan*, 2002]. Some of these dikes feed sand extrudites which apparently reached the seafloor [*Boehm and Moore*, 2002], indicating very shallow emplacement depth. *Phillips* [1990] noted that horizontal intrusions (sills) are most often found near the base of the Santa Cruz mudstone, and therefore probably form early in the burial history. *Jolly and Lonergan* [2002] offer a simple formulation exploring the stress-fluid pressure relationship which would lead to preference for sill emplacement rather than dikes in the deeper portions of the complex, but this approach does not incorporate the role of wall rock heterogeneities or triggering events in driving injection and determining final geometry.

[38] The conditions for burying saturated sand and maintaining the undrained state (due to impermeable wall rock) until it causes failure are very rare [*James et al.*, 2003], and most sedimentary injectite systems are probably better explained by the participation of a catastrophic triggering mechanism [*James et al.*, 2003; *Cartwright et al.*, 2008; *Cartwright*, 2010]. The Monterey Formation wall rocks have weak bedding planes and are tectonically fractured, suggesting potentially high bulk permeability, but we also note that a two-phase pore fluid system as observed in the hydrocarbon-water reservoirs of the Santa Margarita sands can dramatically reduce overall permeability by capillary sealing. An injectite sourced near the maximum burial depth would have to have penetrated more than a kilometer of section to reach the seafloor. Although large injectite systems sometimes exhibit this kind of vertical dimension [*Cartwright*, 2010] it appears that the injections were probably emplaced at shallower depth and were subsequently buried with continued deposition of the Monterey Formation (Santa Cruz mudstone thickness locally reaches 2.7 km [*Stanley*, 1990]).

[39] The Santa Margarita sandstone, source beds for the Yellow Bank Creek Complex, have regionally heterogeneous hydrocarbon concentrations. Outcrops of the intact formation often show contacts between tar-saturated and barren sands, presumably the interfaces between hydrocarbon- and water-saturated sands under burial conditions [*Phillips*, 1990]. When this combined two-phase reservoir was fluidized to form the Yellow Bank Creek Complex, the hydrocarbon-saturated sand and water-saturated sand would be expected to form two distinct slurries with different properties. Under the same driving force, differing viscosities of the aqueous and hydrocarbon fluids would result in different flow rates, separating the injecting slurry into two phases [*Jonk*, 2010] (left side of Figure 8a). During a single injection event, the water-sand slurry flowed more quickly, outpacing the hydrocarbon-saturated sand slurry. This is why, in a single injection, we see textural evidence for hydrocarbon-bearing sand injected into still soft, progressively dewatering sand (Figure 8d). Oil sand "bubbles" crosscut and deform laminations in the sand (Figures 2b, 2f, and 3). The origin of the laminations will be discussed below, but whether they are primary flow banding as suggested by previous authors or form during filtration as we have interpreted, this crosscutting indicates that the hydrocarbon-sand slurry flowed through them after the water-sand had stopped moving.

6.2. Preservation of Emplacement Processes in Observed Fabrics

[40] During sand emplacement, the system must have transitioned from a flowing to geometrically locked grain geometry (the jamming transition; *sensu Corwin et al.* [2005]). In the case of the Yellow Bank Creek Complex, the transition occurred when a sand-water mobile slurry (Figure 8b) decreased in fluid velocity until the grains made contact and locked into a network of framework sand grains with fluid flowing through the pores (Figure 8c). The Yellow Bank Creek Complex contains multiple fabrics, most of which we interpret to have formed either during or after the jamming transition between granular flow and pore fluid diffusion during dewatering.

[41] We observed high apparent porosity in the laminated sandstone. *Thompson et al.* [2007] also observed high apparent porosity, and explained this observation by post-emplacement grain dissolution. The pore spaces in our samples are significantly smaller than grains (Figure 6) so we consider this explanation unlikely although we can not rule out the possibility that some fine fraction was dissolved subsequent to emplacement. *Scott et al.* [2009] measured porosity of the laminated sandstones (mean: 29%), and found lower porosity than our estimates (48% and 51%). However, *Scott et al.*'s [2009] measurements were performed on cemented samples, which under-represent the primary porosity of the sand. They also suggest that porosity at the time of consolidation must have been at least 46%, where 54% is the approximate maximum granular concentration for fluidization [*Leva*, 1959]. Based on this data and the preservation of the delicate laminae and other grain structures, our data are reasonable estimates for the original porosity of the sand just after the jamming transition. *Blower et al.* [2003] showed that for spherical bubbles (we may consider bubbles to be geometrically analogous to grains) following a power law size distribution, 2D grainsizes will underestimate 3D grainsizes. Therefore, our 2D porosity values are likely slight overestimates of 3D porosity.

6.2.1. Textures Relating to Injectite Flow

[42] Wall rock clasts were ripped from the walls during high velocity slurry flow [*Scott et al.*, 2009; *Thompson et al.*, 2007] and can be treated as large, elongate grains in a viscous flow. Previous authors have used terminal settling velocity calculations to bound the minimum upward sand velocity, which requires estimating the density and viscosity of the sand slurry during flow as these quantities are not preserved [e.g., *Duranti and Hurst*, 2004]. *Scott et al.* [2009] used this type of analysis to conclude that the Reynolds numbers of the Yellow Bank Creek Complex during injection required turbulent flow. However, they used fluid viscosity values near that of water [*Kestin et al.*, 1978] and too low for a granular slurry viscosity, as demonstrated by experiments on sediment slurries. We therefore recalculate the Reynolds numbers using a range of viscosities of 1–30 Pa-s [*Major and Pierson*, 1992]. If inertia is potentially important, the appropriate terminal velocity is governed by the balance of inertial drag and buoyancy,

$$U = \sqrt{\frac{4gd(\rho_s - \rho)}{3C_d\rho}} \quad (1)$$

where g is the acceleration due to gravity, d is the diameter of the largest observed clast (0.7 m [*Scott et al.*, 2009]), ρ_s is the grain density (2300 kg/m^3 [*Scott et al.*, 2009]), ρ is the fluid density (1250–1890 kg/m^3 [*Scott et al.*, 2009]) and C_d is the drag coefficient (0.5 for rough spheres). The resultant terminal velocities are 2–4 m/s where the range is provided by the range of densities from dilute to dense suspensions. The Reynolds number is

$$Re = \rho UL/\eta \quad (2)$$

where L is the estimated width of the feeder to the injection (10 m) and η is the range of slurry viscosities from dilute to dense suspensions (1–30 Pa-s). The corresponding range of Reynolds numbers is 1.3×10^3 to 4.9×10^4. Therefore, the turbulent flow inferred by *Scott et al.* [2009] based on scouring of the wall rock was possible during initial transport, but a transition to laminar flow likely occurred as the slurry decelerated and density increased toward the jamming threshold. Whereas sand dikes observed by *Boehm and Moore* [2002] exhibit grain size sorting with coarser grains concentrated toward the center, consistent with laminar flow between the dike walls, the lack of sorting in the large sill at Yellow Bank Beach suggests that well-organized velocity gradients did not persist for long enough to effectively sort the grains. This observation allows that the sand slurry was emplaced as an initially turbulent flow which transitioned to laminar flow behavior during emplacement.

[43] Regardless of initial conditions, the flowing slurry behaved as a laminar flow as the velocity

decreased. Mudstone clasts are gently dipping (17° ± 17°, N = 82) on the outcrop surface, consistent with rotating toward flow lines as the injectite sill flowed horizontally along bedding. Studies of phenocrysts transported in viscous flows have been shown to develop a characteristic alignment parallel with flow direction [*Yamato et al.*, 2012] and sorting of grains by density and shape according to velocity profiles [*Geoffroy et al.*, 2002]. Therefore, we hypothesize that local mudstone clast alignment is the best preserved record of last direction of sand slurry flow during injectite emplacement. We use this alignment as a tentative marker of flow direction, to which we can then compare the other granular features. There can have been almost no relative motion between wall rock clasts and the sand encasing them following emplacement. Any relative rotation would have destroyed laminae microstructures, and this is not observed, so we can assume the orientation we observe is primary (Figure 2c).

[44] The velocity of the slurry eventually declined until the sand stopped moving. This transition, the jamming transition, occurs where particle contacts have sufficient number and strength to stop grains moving relative to one another. The slowing velocity of the slurry reduced the capacity of the flow to suspend the grains, allowing them to settle into contact at the critical porosity. The simulations by *Majmudar et al.* [2007] and experiments by *Wilhelm and Wilmański* [2002] exploring the same transition in the opposite sense (mobilization by pore fluid flow) both indicate that the transition from jammed to unjammed state (stable to flowing or vice verse) is a sudden, threshold transition.

6.2.2. Textures Formed After Jamming

[45] Our observations of crosscutting relationships confirm that the iron oxide-cemented and uncemented laminations are a primary fabric defined by small grain-scale differences [cf. *Scott et al.*, 2009]. The field observations of crosscutting relationships show that the laminae are the earliest-formed fabric in the injectite. They formed prior to large-scale dewatering, as they are deformed by compaction banding and convolute structures (discussed below). The iron oxide cementation exploited this primary fabric. In contrast to *Scott et al.* [2009] we did not detect any packing difference between the laminae types. The only grain-scale difference we detected is a distinction in the apparent aspect ratio of grains. The apparent aspect ratio seen in the 2D thin section is a function of the true aspect ratio and the angle of the grain long axis to the plane of the thin section (rotation about the z-axis, Figure 6). Since the grain size distributions are the same, this suggests the grains were not sorted to form the laminae. We infer that the difference between iron oxide-cemented and uncemented laminae reflects a difference in the degree of alignment, or lineation, of grains within the plane of the laminations, although this distinction can not be directly measured in our 2D sections.

[46] The iron oxide, precipitated from fresh pore water at a later stage after uplift of the marine section, is preferentially concentrated in alternating laminae. Iron oxide cement occurs in the laminae with slightly higher apparent aspect ratio (consistent with stronger shape lineation). We suggest this reflects a difference in the permeability of the laminae, caused by and preserved from the initial orientation of the sand grains, that affected late stage groundwater flow.

[47] We propose that a permeability difference between otherwise similar laminae was established by a percolating fluid rearranging grains immediately following jamming of the granular slurry (Figures 8b and 8c). The apparent 2D porosity (∼50%) is similar to the critical packing densities reported for ellipsoidal grains [*Garboczi et al.*, 1995; *Saar and Manga*, 2002]. Near the critical porosity small variations in porosity or pore geometry give rise to large permeability variations, even with identical grain populations [*Ross et al.*, 2011; *Wilhelm and Wilmański*, 2002]. Permeability is a function of the porosity, as well as geometric details controlling the pore geometry and connectivity, such as grain shape, aspect ratio and orientation, and fluid pressure gradients [*Iverson*, 1997]. In granular material, when the porosity approaches a critical value, parameters that are dependent on porosity, such as permeability, exhibit power law changes in response to small porosity variations. This is the percolation threshold.

[48] We therefore suggest that near the percolation threshold, the pore fluid rearranged grains in such a way to cause the slight alignment contrast between higher and lower permeability laminae. This formed a feedback whereby the flow through relatively high permeability layers was promoted, further rearranging grains and enhancing the permeability difference. Pore fluid drained preferentially into and along the higher permeability layers (Figure 8c). These were the same layers that were later cemented with iron oxide, possibly because of preferred groundwater flow along them.

[49] We propose that the uniform thickness of the laminae reflects a characteristic length scale for the process controlling the permeability instability (laminae thickness, 5.7 ± 1 mm). The length scale was established by the relative contribution of pore fluid advection along the laminae and diffusion across the laminae. We use the length scale to estimate the pore fluid flow velocity from the Péclet number, *P*. The Péclet number is described as

$$P = \frac{UL}{D} \tag{3}$$

where U is the pore fluid velocity (m/s), L is the critical length scale (m, 1/2 laminae width for a relative permeability channel with two walls), and D is the diffusivity (m^2/s, along dewatering pathways as indicated in Figure 8c). The system forms dewatering layers with a spacing perhaps determined by the balance of the advection rate and diffusion rate, i.e. $P = 1$. The hydraulic diffusivity of the sand is dependent on multiple unconstrained factors including *in situ* water content, slurry velocity, and pressure gradients. Therefore we refer to experimental debris flows to determine a reasonable estimate for a moving sand slurry. Based on *Iverson* [1997, Table 8], and assuming that their sand-gravel mixtures were sand dominated (contained high sand concentrations), we estimate the hydraulic diffusivity is on order 10^{-4} m^2/s but allow for an order of magnitude variation. Using the observed average half-width scale of laminae (∼3 mm), we estimate a pore fluid velocity of ∼3 cm/s (permissible range is 3 mm/s–30 cm/s). This is generally consistent with the transport velocity estimates above: in the jammed state, the fluid flow velocity through the porous medium must be significantly less than the emplacement velocity of the fully mobilized flow. Pore fluids traveling at these velocities would exert a flow stress on the grains and potentially rotate those grains that are most loosely held in the granular skeleton, or have the least surrounding grain contacts, imposing a subtle lineation to the preferred conduits. Similar flow velocities (cm/s) are observed to have macroscopic effects on permeability in other natural systems [*Brodsky et al.*, 2003; *Manga et al.*, 2012].

[50] The laminae are accentuated by iron oxide cement. Two previous studies offered conflicting interpretations for the origins of the iron oxide-cemented laminae: *Thompson et al.* [2007] interpreted them as Liesegang banding (a self-organized cyclic variation in concentrations along a gradient) while *Scott et al.* [2009] argued that the cement actually followed a previously existing grain structure. Our results support the interpretation of *Scott et al.* [2009], although our microstructural data indicate that the primary structure highlighted by the iron oxide is not a porosity variation as they suggest, but a more subtle contrast in permeability related to grain orientation and pore shape. We can rule out the Liesegang banding interpretation based on our observations of crosscutting relations. Liesegang rings are precipitated normal to concentration gradients when a precipitation front moves across a homogeneous medium [*Dee*, 1986]. This is most readily observed where they form parallel to joints or concentrically in joint-bounded blocks, nodules, and amygdules, indicating diffusion gradients normal to surfaces of permeability discontinuities in the rock [*McBride*, 2003; *Eichhubl et al.*, 2009]. Our observations show that the iron oxide-cemented laminae are not concentric to fractures or other permeability discontinuities in the rock. They end sharply at the boundaries of dolomite-cemented sands and do not cross regions of homogenous sand where primary grain structures forming the laminae have been destroyed (e.g., convolute structures or small faults).

6.2.3. Textures Resulting From Compaction and Dewatering

[51] After the jamming of the sand grains and formation of the laminae, compaction commenced and the pore water escaped from the injectite. Two classes of features were formed simultaneously by dewatering: 6–13 cm banding, which crosscuts both the dolomite-cemented and laminated sands, and convolute structures, which are observed only in the laminated sand.

[52] The bands represent a spaced compaction fabric, which is primarily horizontal but undulates, possibly in response to topography on the floor of the injectite. *Olsson et al.* [2002] showed that compaction bands form perpendicular to the maximum strain direction, locally reducing permeability. Multiple localization fronts can create trapped fluid in higher porosity zones resulting in an increased pore pressure. *Olsson et al.* [2002] argue that this increased pore pressure will locally decrease the effective mean stress driving compaction and can slow or stop the compaction process. In the Yellow Bank Creek Complex, the increased pore pressure between compaction bands was released by localized fluid venting in pipes which deformed or destroyed laminae, forming the convolute structures. The geometry and spacing of the convolute structures

strongly resemble fumarolic pipes formed in compacting ash flows, where material is also well mixed and microstructure destroyed along the upward flow path [*Nermoen et al.*, 2010], as well as pipes, consolidation laminae and burst through structures associated with water escape from saturated sediments.

[53] In areas of the injectite where compaction bands are weakly expressed or absent, convolute structures grew much taller and are more widely spaced (Figure 5b). These may have facilitated the draining of larger volumes of water. In the southern part of the outcrop, where dolomite-cemented sand forms vertical columns (Figure 3), tall, isolated convolutions are more abundant. This may record vertical motion of the sand during upward emplacement. Toward the northern part of the outcrop, where the subhorizontal compaction bands are strongly developed, the convolutions are short and closely spaced, and lean toward the north, as do the "fingers" of oil sand injected into the wet sand (Figure 3a). This may record a component of subhorizontal flow during injection of the sill, and the continued lateral momentum during initial dewatering and compaction. Convolutions and areas of wiped-out laminae are also found immediately below mudstone clasts. This may indicate that fluid pressure was locally elevated due to the mudstone clast blocking upward fluid escape.

7. Summary and Conclusions

[54] The Yellow Bank Creek Complex is a natural example of the subsurface mass movement of a sand slurry and preserves textures that provide insight into the dynamics of injection in the rock record. Numerous textural features are evident in the exposure of the injectite. From field and microstructural observations we show that many of these textures are formed during the jamming transition and dewatering of the mobilized sands. We conclude that injectite formation involved the following processes:

[55] 1. Elevated pore fluid pressure combined with a trigger event, likely seismic shaking, fluidized and emplaced the granular slurry upsection in two separate phases (aqueous and hydrocarbon) through fractures in the mudstone hostrock.

[56] 2. Clasts of mudstone were entrained in the granular slurry, the long axes of which likely aligned with laminar flow paths as slurry velocity waned.

[57] 3. The granular slurry velocity dropped and could no longer suspend grains, creating a jammed granular framework. Pore waters reorganized grains creating a primary fabric composed of alternating laminae of more and less well aligned grains. Porosities were sufficiently high that slight differences in grain organization resulted in large variations in permeability.

[58] 4. The higher viscosity of hydrocarbon slurry allowed it to continue to flow during aqueous slurry dewatering, intruding the recently injected and jammed sand, crosscutting and deforming the laminae microtextures.

[59] 5. Compaction of the system occurred creating compaction bands and convolute dewatering structures.

[60] 6. Later, two separate cements were formed: dolomitization of the hydrocarbon sands, and iron oxide preferentially precipitated in high permeability laminae in the aqueous sand.

[61] The conditions of "jamming" of this sand injectite during emplacement are preserved in the spacing of the laminae, controlled by the velocity of the pore fluid at the moment of grain lock-up. This transient condition created a fabric which persists in the sandstone and affects pore water flow as evidenced by the differential cementation of alternating laminae. In the Yellow Bank Creek Complex, these laminae are highlighted by iron oxide cement, but without differential cementation they are very difficult to distinguish by microstructural observations alone and it is unlikely that they would be detected. We speculate that similar textures may be present in other sand deposits emplaced by granular flow processes, and may have noticeable effects on permeability anisotropy.

Acknowledgments

[62] Casey Moore, Bob Garrison and Hilde Schwartz are thanked for introducing us to this outcrop and for very helpful discussions. We thank Michael Manga and Bob Behringer for discussions on granular flow behaviors. Greg Larson helped with data collection in the field. Nicholas van der Elst and Kena Fox-Dobbs are acknowledged for discussions on statistics. This research was supported by NSF MARGINS Fellowship OCE-0840977 to E. E. Brodsky and C. Rowe. J. Kirkpatrick was supported by NSF EAR (Award 0948740).

References

Addicott, W. O. (1972), Provincial middle and late Tertiary molluscan stages, Temblor Range, California, in *Society of*

Economic Paleontologists and Mineralogists, Pacific Section, Proceedings of the Pacific Coast Miocene Biostratigraphic Symposium, Bakersfield, California, pp. 1–26, Soc. of Econ. Paleontol. and Mineral., Los Angeles, Calif.

Aiello, I. W. (2005), Fossil seep structures of the Monterey Bay region and tectonic/structural controls on fluid flow in an active transform margin, *Palaeogeogr. Palaeoclimatol. Palaeoecol.*, *227*, 124–142.

Bjørk, T. E., K. Mair, and H. Austrheim (2009), Quantifying granular material and deformation: Advantages of combining grain size, shape, and mineral phase recognition analysis, *J. Struct. Geol.*, *31*, 637–653.

Blower, J., J. Keating, H. Mader, and J. Phillips (2003), The evolution of bubble size distributions in volcanic eruptions, *J. Volcanol. Geotherm. Res.*, *120*(1–2), 1–23, doi:10.1016/S0377-0273(02)00404-3.

Boehm, A., and J. C. Moore (2002), Fluidized sandstone intrusions as an indicator of paleostress orientation, Santa Cruz, California, *Geofluids*, *2*, 147–161.

Bramlette, M. N. (1946), The Monterey formation of California and the origin of its siliceous rocks, *U.S. Geol. Surv. Prof. Pap.*, *212*, 93 pp.

Brodsky, E., E. Roeloffs, D. Woodcock, I. Gall, and M. Manga (2003), A mechanism for sustained groundwater pressure changes induced by distant earthquakes, *J. Geophys. Res.*, *108*(B8), 2390, doi:10.1029/2002JB002321.

Cartwright, J. (2010), Regionally extensive emplacement of sandstone intrusions: A brief review, *Basin Res.*, *22*, 502–516.

Cartwright, J., M. Huuse, and A. Aplin (2007), Seal bypass systems, *AAPG Bull.*, *91*(8), 1141–1166.

Cartwright, J., D. James, M. Huuse, W. Vetel, and A. Hurst (2008), The geometry and emplacement of conical sandstone intrusions, *J. Struct. Geol.*, *30*, 854–867.

Clark, J. C. (1981), Stratigraphy, paleontology, and geology of the central Santa Cruz Mountains, California Coast Ranges, *U.S. Geol. Surv. Prof. Pap.*, *1168*, 51 pp.

Corwin, E. I., H. M. Jaeger, and S. R. Nagel (2005), Structural signature of jamming in granular media, *Nature*, *435*, 1075–1078, doi:10.1038/nature03698.

Davies, R. J., M. Huuse, P. Hirst, J. Cartwright, and Y. Yang (2006), Giant clastic intrusions primed by silica diagenesis, *Geology*, *34*, 917–920, doi: 10.1130/G22937A.1.

Davies, R. J., N. R. Goulty, and D. Meadows (2008), Fluid flow due to the advance of basin-scale silica reaction zones, *Geol. Soc. Am. Bull.*, *120*(1–2), 195–206.

Dee, G. T. (1986), Patterns produced by precipitation at a moving reaction front, *Phys. Rev. Lett.*, *57*(3), 271–278.

Duranti, D., and A. Hurst (2004), Fluidization and injection in the deep-water sandstones of the Eocene Alba Formation (UK North Sea), *Sedimentology*, *51*, 503–529, doi:10.1111/j.1365-3091.2004.00634.x.

Eichhubl, P., N. C. Davatzes, and S. P. Becker (2009), Structural and diagenetic control of fluid migration and cementation along the Moab fault, Utah, *AAPG Bull.*, *93*(5), 653–681.

El-Sabbagh, D., and R. E. Garrison (1990), Silica diagenesis in the Santa Cruz mudstone (upper Miocene), La Honda Basin, California, in *Geology and Tectonics of the Central California Coastal Region, San Francisco to Monterey*, vol. 67, edited by R. E. Garisson et al., pp. 123–132, Am. Assoc. of Pet. Geol., Bakersfield, Calif.

Garboczi, E. J., K. A. Snyder, J. F. Douglas, and M. F. Thorpe (1995), Geometrical percolation threshold of overlapping ellipsoids, *Phys. Rev. E*, *52*, 819–828.

Geoffroy, L., J. P. Callot, C. Aubourg, and M. Moreira (2002), Magnetic and plagioclase linear fabric discrepancy in dykes: A new way to define the flow vector using magnetic foliation, *Terra Nova*, *14*(3), 183–190, doi:10.1046/j.1365-3121.2002.00412.x.

Graham, S. A., and L. A. Williams (1985), Tectonic, depositional and diagenetic history of Monterey Formation (Miocene), central San Joaquin Basin, California, *AAPG Bull.*, *69*, 385–411.

Gross, M. R. (1995), Fracture partitioning: Failure mode as a function of lithology in the Monterey Formation of coastal California, *Geol. Soc. Am. Bull.*, *107*(7), 779–792.

Hubbard, S. M., B. W. Romans, and S. A. Graham (2007), An outcrop example of large-scale conglomeritic intrusions sourced from deep-water channel deposits, Cerro Toro Formation, Magallanes basin, southern Chile, in *Sand Injectites: Implications for Hydrocarbon Exploration and Production*, edited by A. Hurst and J. Cartwright, *AAPG Mem.*, 87, 199–207.

Hurst, A., and J. Cartwright (2007), Relevance of sand injectites to hydrocarbon production and exploration, in *Sand Injectites: Implications for Hydrocarbon Exploration and Production*, *AAPG Mem.*, *87*, 1–19.

Hurst, A., J. Cartwright, M. Huuse, R. Jonk, A. Schwab, D. Duranti, and B. Cronin (2003), Significance of large-scale sand injectites as long-term fluid conduits: Evidence from seismic data, *Geofluids*, *3*, 263–274.

Huuse, M., C. A.-L. Jackson, P. van Rensbergen, R. J. Davies, P. B. Flemings, and R. J. Dixon (2010), Subsurface sediment remobilization and fluid flow in sedimentary basins: An overview, *Basin Res.*, *22*, 342–360, doi: 10.1111/j.1365-2117.2010.00488.x.

Iverson, R. M. (1997), The physics of debris flows, *Rev. Geophys.*, *35*(3), 245–296.

James, D. M. D., R. Jolly, and L. Lonergan (2003), Discussion on mechanisms and controls on the formation of sand intrusions, *J. Geol. Soc. London*, *160*, 495–496.

Jolly, R. J. H., and L. Lonergan (2002), Mechanisms and controls on the formation of sand intrusions, *J. Geol. Soc.*, *159*, 605–617, doi: 10.1144/0016-764902-025.

Jonk, R. (2010), Sand-rich injectites in the context of short-lived and long-lived fluid flow, *Basin Res.*, *22*, 603–621, doi:10.1111/j.1365-2117.2010.00471.x.

Jonk, R., J. Parnell, and A. Hurst (2005), Aqueous and petroleum fluid flow associated with sand injectites, *Basin Res.*, *17*, 241–257, doi:10.1111/j.1365-2117.2005.00262.x.

Kane, I. A. (2010), Development and flow structures of sand injectites: The Hind Sandstone Member injectite complex, Carboniferous, UK, *Mar. Pet. Geol.*, *27*, 1200–1215.

Kazerouni, A. M., H. Friis, J. B. Svendsen, and R. Weibel (2011), Heavy mineral sorting in downwards injected Palaeocene sandstone, Siri Canyon, Danish North Sea, *Sediment. Geol.*, *236*, 279–285.

Keehm, Y., T. Mukerji, and A. Nur (2004), Permeability prediction from thin sections: 3D reconstruction and Lattice-Bolzmann flow simulation, *Geophys. Res. Lett.*, *31*, L04606, doi:10.1029/2003GL018761.

Kestin, J., M. Sokolov, and W. A. Wakeham (1978), Viscosity of liquid water in the range −8 degc to 150 degc, *J. Phys. Chem. Ref. Data*, *7*, 941–948, doi:10.1063/1.555581.

Leva, M. (1959), *Fluidization*, McGraw-Hill, New York.

Levi, T., R. Weinberger, T. Aïfa, Y. Eyal, and S. Marco (2006), Earthquake-induced clastic dikes detected by anisotropy of magnetic susceptibility, *Geology*, *34*(2), 69–72, doi:10.1130/G22001.1.

Levi, T., R. Weinberger, Y. Eyal, and V. Lyakhovsky (2008), Velocities and driving pressures of clay-rich sediments injected into clastic dykes during earthquakes, *Geophys. J. Int.*, *175*(3), 1095–1107.

Levi, T., R. Weinberger, and Y. Eyal (2011), A coupled fluid-fracture approach to propagation of clastic dikes during earthquakes, *Tectonophysics*, *498*, 35–44.

Long, H., R. Swennen, A. Foubert, M. Dierick, and P. Jacobs (2009), 3D quantification of mineral components and porosity distribution in Westphalian C sandstone by micro-focus X-ray computed tomography, *Sediment. Geol.*, *220*, 116–125.

Majmudar, T. S., M. Sperl, S. Luding, and R. P. Behringer (2007), Jamming transition in granular systems, *Phys. Rev. Lett.*, *98*, 058001, doi:10.1103/PhysRevLett.98.058001.

Major, J. J., and T. C. Pierson (1992), Debris flow rheology: Experimental analysis of fine-grained slurries, *Water Resour. Res.*, *28*(3), 841–857, doi:10.1029/91WR02834.

Manga, M., I. Beresnev, E. Brodsky, J. Elkhoury, D. Elsworth, S. Ingebritsen, D. Mays, and C. Wang (2012), Changes in permeability caused by transient stresses: field observations, experiments, and mechanisms, *Rev. Geophys.*, *50*, RG2004, doi:10.1029/2011RG000382.

McBride, E. F. (2003), Pseudofaults resulting from compartmentalized liesegang bands: Update, *Sedimentology*, *50*(4), 725–730.

Minisini, D., and H. Schwartz (2006), An early Paleocene cold seep system in the Panoche and Tumey Hills, Central California, (United States), in *Sand Injectites: Implications for Hydrocarbon Exploration*, *AAPG Mem.*, 87, 185–198.

Nermoen, A., O. Galland, E. Jettestuen, K. Fristad, Y. Podladchikov, H. Svensen, and A. Malthe-Sørenssen (2010), Experimental and analytic modeling of piercement structures, *J. Geophys. Res.*, *115*, B10202, doi:10.1029/2010JB007583.

Olsson, W. A., D. J. Holcomb, and J. W. Rudnicki (2002), Compaction localization in porous sandstone: Implications for reservoir mechanics, *Oil Gas Sci. Technol.*, *57*, 591–599.

Phillips, R. L. (1981), Depositional environments of the Santa Margarita Sandstone in the Santa Cruz Mountains, California, PhD dissertation, 358 pp., Univ. of Calif., Santa Cruz, Calif.

Phillips, R. L. (1990), Depositional and structural controls on the distribution of tar sands in the Santa Cruz Mountains, California, in *Geology and Tectonics of the Central California Coastal Region, San Francisco to Monterey*, vol. 67, edited by R. E. Garisson et al., pp. 105–121, Am. Assoc. of Pet. Geol., Bakersfield, Calif.

Rodrigues, N., P. R. Cobbold, and H. Løseth (2009), Physical modelling of sand injectites, *Tectonophysics*, *474*, 610–632.

Ross, J. A., J. Peakall, and G. Keevil (2011), An integrated model of extrusive sand injectites in cohesionless sediments, *Sedimentology*, *58*, 1693–1715, doi:10.1111/j.1365-3091.2011.01230.x.

Saar, M. O., and M. Manga (2002), Continuum percolation for randomly oriented soft-core prisms, *Phys. Rev. E*, *65*, 056131.

Schwartz, H., J. C. Sample, K. Weberling, D. Minisini, and J. C. Moore (2003), An ancient linked fluid migration system: Cold-seep deposits and sandstone intrusions in the Panoche Hills, California, USA, *Geo Mar. Lett.*, *23*, 340–350.

Scott, A., M. Vigorito, and A. Hurst (2009), The process of sand injection: Internal structures and relationships with host strata (Yellowbank Creek Injectite Complex, California, USA), *J. Sediment. Res.*, *79*(8), 568–583.

Stanley, R. G. (1990), Evolution of the Tertiary La Honda Basin, central California, in *Geology and Tectonics of the Central California Coastal Region, San Francisco to Monterey, Guidebook*, vol. 67, edited by R. E. Garisson et al., pp. 1–29, Am. Assoc. of Pet. Geol., Bakersfield, Calif.

Stanley, R. G., and P. G. Lillis (2000), Oil-bearing rocks of the Davenport and Point Reyes Areas and their implications for offset along the San Gregorio and Northern San Andreas Faults, in *Proceedings of the 3rd Conference on Tectonic Problems of the San Andreas Fault System*, edited by R. Kovich, p. 14, Stanford Univ. Press, Standford, Calif.

Thompson, B. J., R. E. Garrison, and J. C. Moore (1999), A late Cenozoic sandstone intrusion west of Santa Cruz, California: Fluidized flow of water- and hydrocarbon-saturated sediments, in *Late Cenozoic Fluid Seeps and Tectonics Along the San Gregorio Fault Zone in the Monterey Bay Region, California*, vol. GB-16, edited by R. E. Garrison et al., pp. 53–747, Am. Assoc. of Pet. Geol., Bakersfield, Calif.

Thompson, B. J., R. E. Garrison, and J. C. Moore (2007), A reservoir-scale Miocene injectite near Santa Cruz, California, in *Sand Injectites: Implications for Hydrocarbon Exploration and Production*, *AAPG Mem.*, 87, 151–162.

Vigorito, M., and A. Hurst (2010), Regional sand injectite architecture as a record of pore-pressure evolution and sand redistribution in the shallow crust: Insights from the Panoche Giant Injection Complex, California, *J. Geol. Soc.*, *167*, 889–904, doi:10.1144/0016-76492010-004.

Vigorito, M., A. Hurst, J. Cartwright, and A. Scott (2008), Regional-scale subsurface sand remobilization: Geometry and architecture, *J. Geol. Soc.*, *165*, 609–612.

Wilhelm, T., and K. Wilmański (2002), On the onset of flow instabilities in granular media due to porosity inhomogeneities, *Int. J. Multiphase Flow*, *28*, 1929–1944.

Yamato, P., R. Tartése, T. Duretz, and D. May (2012), Numerical modelling of magma transport in dykes, *Tectonophysics*, *526–529*, 97–109, doi:10.1016/j.tecto.2011.05.015.